Earthquake Research Advances 5 (2025) 100375

Contents lists available at ScienceDirect

Earthquake Research Advances

journal homepage: www.keaipublishing.com/en/journals/earthquake-research-advances

Seismogenic characteristics of the 2025 Dingri M_s 6.8 earthquake: Insights from GNSS observations

Yu Li *, Yuebing Wang, Yinxing Shao, Hongbo Shi, Tan Wang

China Earthquake Networks Center, China Earthquake Administration, Beijing, 100045, China

ARTICLE INFO

Keywords:
Dingri M_s6.8 earthquake
GNSS
GAMIT/GLOBK
Pre- and co-seismic deformation

ABSTRACT

This study investigates the seismogenic characteristics of the 2025 Dingri M_S 6.8 earthquake through multi-parametric GNSS analyses of velocity field, strain rate evolution and displacement patterns across pre-seismic and co-seismic phases. Our findings demonstrate spatiotemporally heterogeneous crustal deformation exhibiting kinematic precursors correlating with subsequent rupture propagation. The epicentral region exhibited prolonged N-S compressional strain accumulation accompanied by accelerated E-W extensional deformation and progressive counterclockwise rotation of principal strain axes three years prior, indicating enhanced local normal fault activities. Co-seismic observations delineate significant displacement domains, with the XZSJ (~95 mm) site documenting the largest northeastward motion, consistent with rupture propagation along secondary N-E trending structures. Co-seismic strain analysis identifies concentrated seismic moment release primarily west of the Xainza-Dinggye Fault and north of the Southern Qinghai-Xizang Detachment Fault system, displaying normal fault kinematics in agreement with the seismic source mechanism. The co-seismic strain partitioning pattern shows critical implications for regional N-S trending normal fault system, necessitating sustained geodetic monitoring to advance understanding of seismic cycle deformation in this area.

1. Introduction

On January 7, 2025 at 09:05:16 Beijing time (01:05:16 UTC), a M_S 6.8 earthquake struck Dingri County, Shigatse City, Xizang Autonomous Region, China (28.50°N, 87.45°E), with a focal depth of 10 km (Fig. 1). By February 10, 2025 at 16:00, a total of 9 451 aftershocks had been recorded (https://www.cenc.com.cn). This high-magnitude and intense earthquakes resulted in the tragic loss of 126 lives, damage to over 240 000 houses, affected approximately 139 000 people to varying degrees, and resulted in direct economic losses of 8.945 billion Yuan (https://www.mem.gov.cn/).

Following the earthquake, numerous research institutions and scholars employed various methods and datasets to investigate the source mechanism and rupture process. They concluded that this event was a typical normal fault tensile earthquake (Shi et al., 2025; Wang et al., 2025). The earthquake exhibited asymmetric bilateral rupture propagation along primarily extending northward over a distance of approximately 50 km. Field investigations and satellite imagery revealed a surface rupture of about 25 km (Shi et al., 2025). Combining field rupture data with InSAR coseismic results (Wang et al., 2025), it was inferred that the causative fault was the Dengmocuo Fault (DMCF). The DMCF, as the main boundary fault on the eastern edge of the Dengmoco Graben, one of the larger grabens in the southern part of the Xainza-Dinggye Rift, has been active since the 2015 Nepal M_W 7.8 Gorkha earthquake, with ten earthquakes of M 5.0 or higher occurring successively (https://www.eq-igl.ac.cn).

Despite these advances, critical knowledge gaps persist regarding the deformation characteristics of the regional crust before and during the Dingri M_S 6.8 earthquake, especially the co-seismic strain partitioning mechanisms. This paper analyzes the pre-seismic crustal deformation characteristics from two key sessions: 1999–2022 and 2022–2024. We integrate high-frequency (1 Hz) and conventional (30 s) GNSS observations to resolve both kenimatics rupture processes and static displacement fields of the Dingri M_S 6.8 earthquake. Our comprehensive analysis of those results aims to provide new constraints on studying earthquake incubation and co-seismic rupture processes in the future.

2. Tectonic background

As a region with the most intense modern tectonic and seismic activities in China (Tapponnier et al., 1982), the Qinghai-Xizang

* Corresponding author.
E-mail address: yli@seis.ac.cn (Y. Li).

Peer review under the responsibility of Editorial Board of Earthquake Research Advances.

https://doi.org/10.1016/j.eqrea.2025.100375
Received 21 February 2025; Received in revised form 21 March 2025; Accepted 24 March 2025

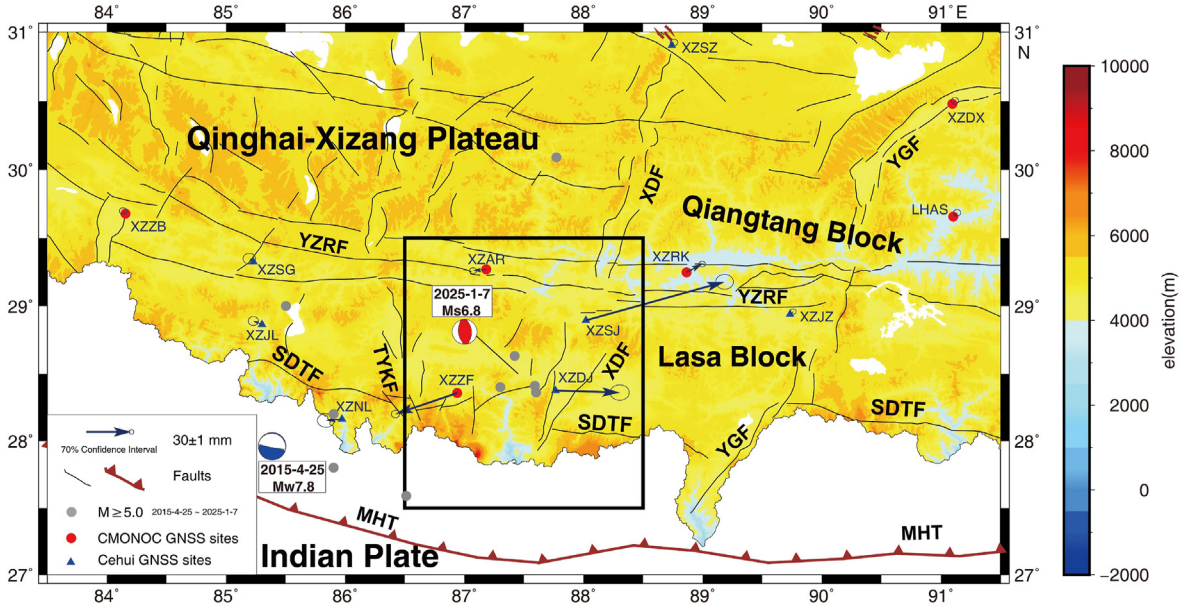

Fig. 1. Regional tectonic background map and the co-seismic displacement of Dingri M_S 6.8 earthquake. Red and blue beach balls represent the epicenters of Dingri M_S 6.8 earthquake and Nepal M_W 7.8 earthquake, and the focal mechanisms are based on the published results by the global centroid moment tensor project (GCMT, http://www.globalcmt.org). The solid black and brown lines represent active faults, based on data from the National Seismically Active Fault Exploration Data Center (http://www.activefault-datacenter.cn), and the fault name abbreviations are as follows: MHT−Main Himalayan Thrust Fault, YZRF−Yarlung Zangbo River Fault, XDF−Xainza-Dinggye Fault, STDF−Southern Qinghai-Xizang Detachment Fault system, YGF−Yadong-Gulu Fault, TYKF−Tangra Yunco-Kongco Fault. The black box indicates the range of GNSS sites framed by the follow-up study of this paper.

(Qingzang) Plateau has a large number of active faults in and around it, which control the regional strong seismic activities. At the collision zone between the Indian and Eurasian plates, two large-scale extensional structures have formed: the Southern Qingzang Detachment Fault system (STDF) and the Yarlung Zangbo River Fault zone (YZRF) (Liu et al., 2015). The region between these structures, subjected to E-W tensile forces, has developed a series of nearly equally spaced N-S faults, making it prone to shallow normal fault earthquakes. According to studies of the M_W 7.8 Gorkha earthquake in Nepal on April 25, 2015, this event applied a coulomb stress of more than 0.01 MPa to the Xainza-Dinggye Fault system (XDF), potentially accelerating large earthquake activities in the southern Qingzang normal fault system (Sheng et al., 2015). Since then, over ten earthquakes with magnitudes greater than 5.0 have occurred in this area, including the M_S 5.9 Dingri earthquake on March 20, 2020 (https://eq-igl.ac.cn/zhxw/info/2025/38560.html).

The DMCF, a southern branch of the west limb of the XDF, extends approximately 60 km. This earthquake produced a surface rupture zone about 25 km long, starting from Qiangga Village in Changso Township in the south and ending at Yangmudingco in the north. The surface rupture zone consists mainly of discontinuous or oblique tensional fissures and scarps, accompanied by minor compressive bulges, exhibiting distinct segmental characteristics (Shi et al., 2025).

3. GNSS data

The GNSS data used in this study are differentiated based on application scenarios and consist of two parts: 1) Raw GNSS data (Domestic) primarily come from the GNSS reference sites and regional sites of the Crustal Motion Observation Network of China (CMONOC) project Phase-I/II, and the continuous GNSS sites of the Xizang Institute of Basic Surveying and Mapping (XZISM); 2) Horizontal velocity field data (Overseas) are sourced from Wang and Shen (2020), as detailed in Table 1.

The high-frequency GNSS data employed in this paper consist of 15 min spanning from 01:00:00 to 01:14:59 UTC on January 7, 2025. For co-seismic permanent deformation analysis, we utilized 30 s sampled GNSS observations collected during a four-day period encompassing three days before the earthquake and one day after the earthquake, namely from January 4 to January 7, 2025 (UTC time).

4. Pre-seismic deformation characteristics

4.1. GNSS data processing

This study systematically compiled and processed GNSS data from the reference and regional sites of CMONOC spanning the period 1999 to 2024. Through rigorous analysis using the GAMIT module of the GAMIT/GLOBK 10.71 software suite (Herring et al., 2018), original carrier phase observations were processed to derive double-difference solutions. The processing protocol incorporated critical error mitigation strategies including: satellite and receiver clock bias estimation, tropospheric delay correction, ionospheric correction, solid earth tide corrections, etc. (Li, 2021). This comprehensive approach yielded daily loosely constrained solutions containing site coordinates, polar motion parameters, satellite orbital elements, and tropospheric zenith delays, accompanied by their corresponding variance-covariance matrices. For enhanced geodetic

Table 1
Data sources and information.

Num.	Application Scenarios	Attribution	Period	Observation frequency	Region
1	Pre-seismic	CMONOC	1997–2024	30 s	Domestic
		Wang and Shen (2020)	1997–2016	30 s	Overseas
2	Co-seismic	CMONOC	01:00:00~01:14:59/2025-1-4~2025-1-7	1 HZ/30 s	Domestic
		XZISM	01:00:00~01:14:59/2025-1-4~2025-1-7	1 HZ/30 s	Domestic

referencing, the GLOBK module was subsequently employed to perform network adjustment through the integration of regional daily solutions with global daily solutions. This adjustment utilized 55 globally distributed IGS sites as reference sites, ensuring alignment with the International Terrestrial Reference Frame 2020 (ITRF2020) (Altamimi et al., 2023b). The final output comprised position time series for all GNSS sites rigorously aligned to the ITRF2020 framework, providing fundamental data for crustal deformation analysis.

For isolated outliers present in the raw GNSS position time series, we implemented a systematic detection and elimination protocol using the Interquartile Range (IQR) criterion (Whaley, 2005). To address clustered anomalies typically arising from instrumental variations or antenna height measurement errors, we developed a comprehensive correction strategy involving data rectification followed by specialized reprocessing procedures. This dual-method approach ensures robust anomaly mitigation while preserving the integrity of geospatial-temporal patterns in the dataset.

4.2. GNSS velocity field

Based on the GNSS site position time series model (Nikolaidis, 2002; Bock and Melgar, 2016), we performed least squares estimation to fit the original position time series for each GNSS site. To investigate pre-seismic crustal deformation characteristics, the study period was divided into two segments (1997–2022 and 2022–2024) following GNSS annual consultation requirements. During data processing, we accounted for co-seismic and post-seismic effects of earthquakes with $M \geq 6.0$ occurring within the period. This analysis yielded two key velocity fields: a long-term stable crustal movement background and a short-term pre-seismic crustal movement velocity field. For overseas regions, velocity field results from Wang and Shen (2020) were transformed into the ITRF2020 frame using official transformation parameters from the ITRF website (https://itrf.ign.fr/en/solutions/transformations). To facilitate tectonic interpretation, all horizontal velocity fields in ITRF2020 were further converted to the stable Eurasian plate reference frame using Euler

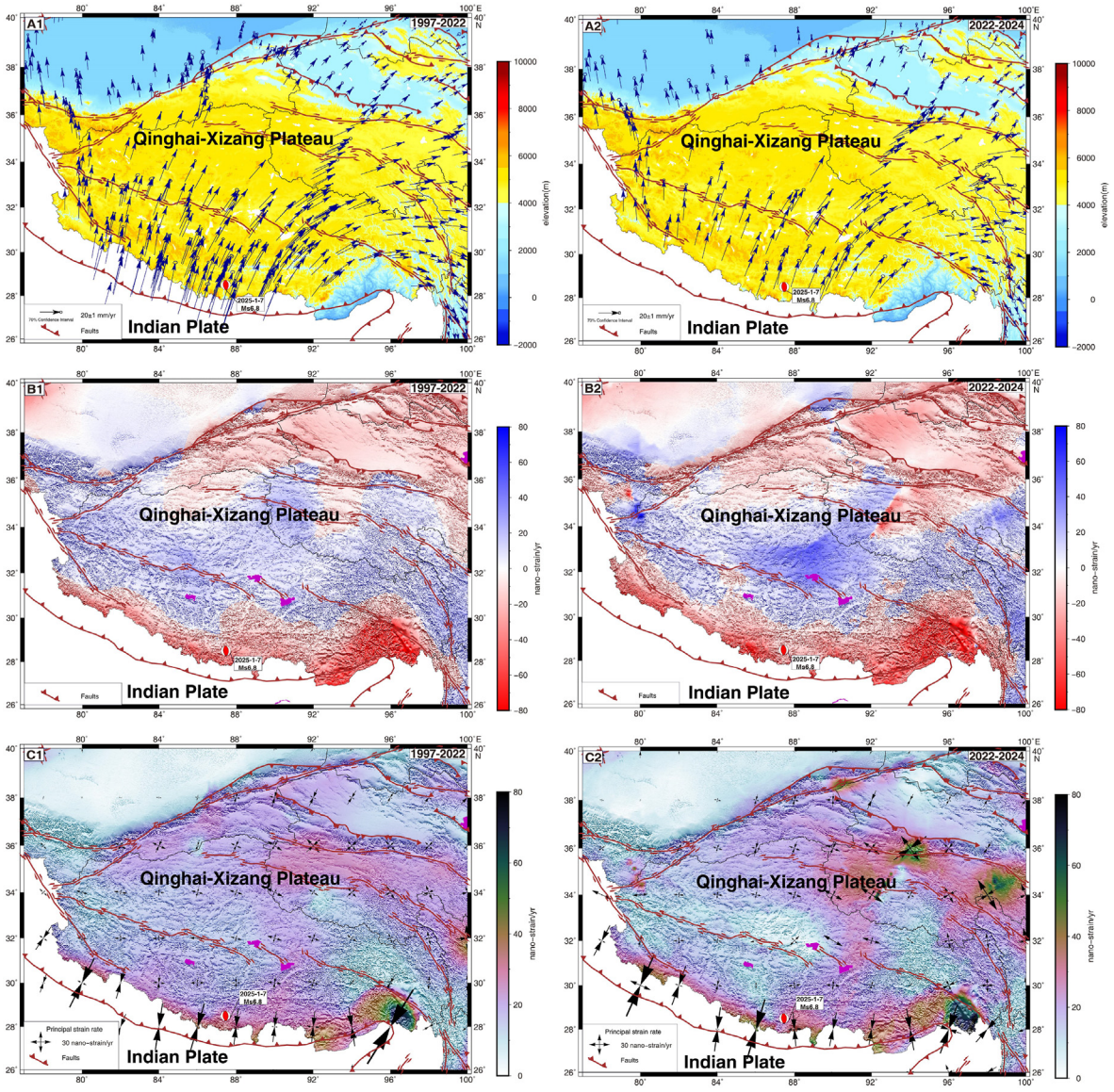

Fig. 2. The pre-seismic GNSS horizontal velocity field with respect to stable Eurasian plate and strain rate field. A1-A2 indicat the regional GNSS horizontal velocity field corresponding to the two periods, B1-B2 represent the regional surface dilatation rates, and C1-C2 show the regional maximum shear strain rate with the principal strain rate corresponding to the two periods. Blue arrows indicate GNSS velocities from this study (Domestic) and previous study (Overseas, quoted from Wang and Shen (2020). Error ellipses represent 70% confidence. Black cross arrow indicates the principal strain rate drived from GNSS velocity field. Other symbols are same as Fig. 1.

pole parameters provided by Altamimi et al. (2023a).

Notably, sites exhibiting velocity deviations exceeding 3σ from neighboring sites and located away from active boundaries with steep velocity gradients were identified as outliers using the VISR3 interpolation method (Shen et al., 2000). Except for the aforementioned special tectonic domains, the crustal deformation pattern of other region of Qingzang Plateau conforms to a continuous deformation regime (Wang and Shen, 2020). This approach estimates continuous deformation fields by interpolating velocities from surrounding sites while excluding the target site's own observed velocity. Through this quality control process, we derived a refined horizontal velocity field for the Qingzang Plateau and adjacent regions (Fig. 2).

From panels A1-A2 in Fig. 2, it can be seen that the Main Himalayan Thrust fault (MHT) in southern Qingzang demonstrates ~40 mm/yr NNE motion, consistent with its role as the leading edge of plate collision. After crossing the YZRF to the north, this rate diminishes to ~20 mm/yr. Distinct kinematic patterns near the Himalaya's eastern and western structural nodes reveal the plateau's dominant N-S shortening superimposed on E-W extension. Both velocity field periods indicate sustained high NE motion rates in the epicentral region prior to the earthquake.

4.3. GNSS strain rate field

To address structural deformation characterization near the epicenter and mitigate spatial sampling biases, we calculated horizontal crustal strain rate fields using the slip inversion method based on the continuous strain field proposed by Shen et al. (1996, 2015) and Jackson et al. (1997). This approach ensures solution stability, mitigates edge effects, and maintains robust performance, particularly advantageous for strain field computation in medium-to-small scale regions.

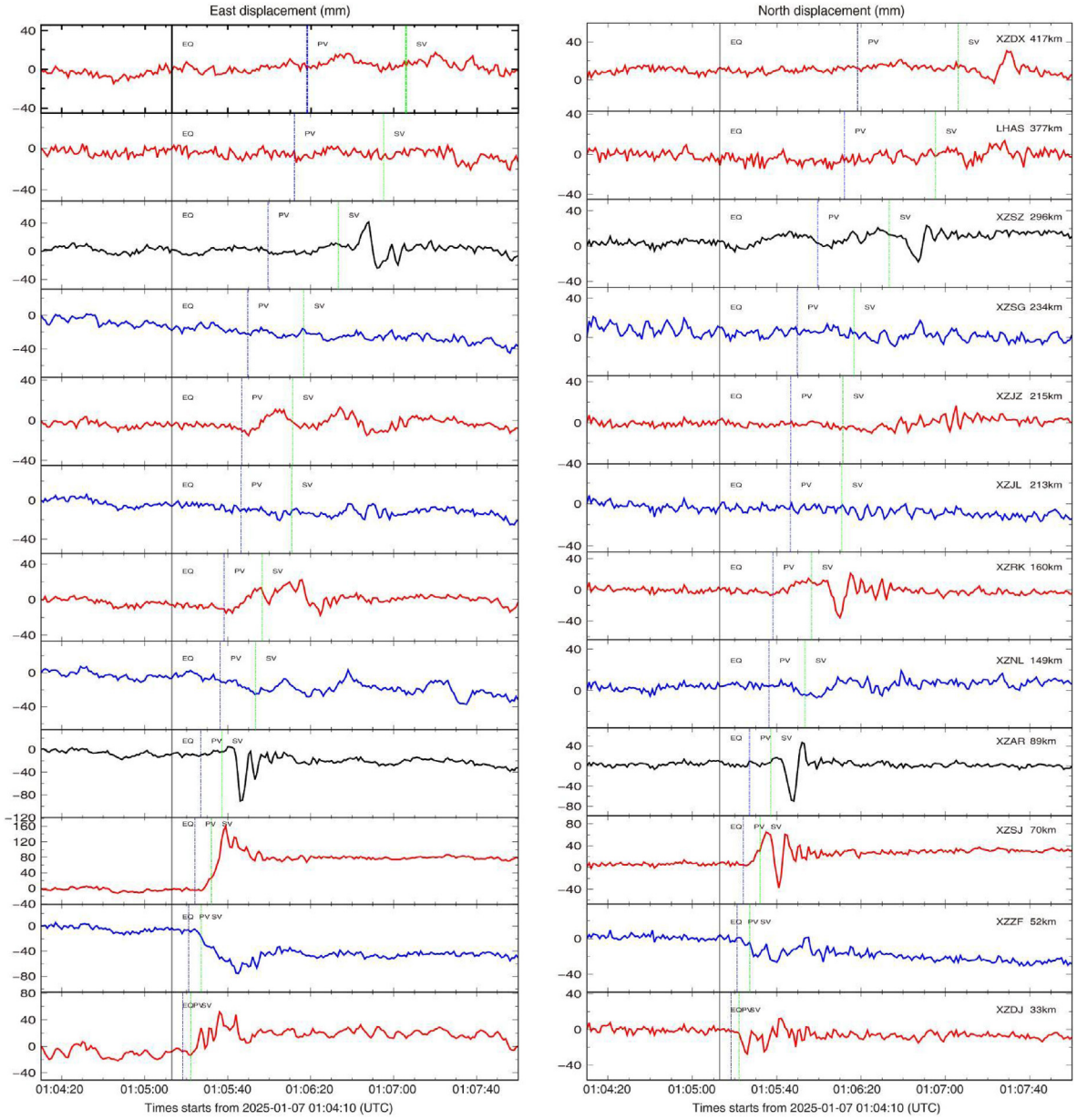

Fig. 3. Examples of displacement waveforms of kinematic response during earthquake recorded by GNSS sites. The x-axis represents time (unit: s); The black, red and blue solid lines respectively represent the kinematic response displacement waveform recorded by the sites located on the north, east and west sides of the epicenter. The code and number in the upper right corner are the site code and epicentral distances in km. The black vertical solid line represents the time of the earthquake (2025-01-07 01:05:16 UTC, EQ), while the vertical dotted line represents the time when P (blue, PV) and S waves (green, SV) arrive at each site calculated by the TAUP software (Crotwell et al., 1999) using standard models.

Panels B1-B2 and C1-C2 in Fig. 2 systematically illustrate surface dilatation rates, maximum shear strain rates with principal strain rates across respective observation periods. Three principal deformation patterns emerge: (1) Southern Qingzang exhibits persistent compressional deformation orthogonal to the MHT, accompanied by substantial shear strain partitioning. (2) The epicenteral region demonstrates intensified E-W extension with counterclockwise (CCW) rotation of principal compressive strain axes during the triennium preceding the seismic event. (3) The Bayan Har block reveals accelerated shear strain accumulation with westward CCW rotation in principal compressive strain orientations, indicative of progressive crustal strain localization.

Furthermore, the observed strain patterns show kinematic consistency with documented normal faulting reactivation, suggesting possible pre-seismic fracture system activation. The identified strain acceleration in the Bayan Har block necessitates intensified geodetic surveillance due to its implications for regional strain energy accumulation.

5. Co-seismic deformation characteristics

5.1. Kinematic deformation characteristics

In this study, we also processed 1 Hz GNSS data from sites near the epicenter using the GAMIT/GLOBK 10.71 software suite (Herring et al., 2018) through differential positioning methodology. Detailed processing procedures and strategies follow the framework described in Li et al. (2024). The TRACK module's relative positioning approach necessitated the selection of reference sites with optimal observational quality and minimal seismic influence. Preliminary co-seismic displacement analysis through significance testing revealed concentrated seismic effects within a 300 km radius of the epicenter. Consequently, we designated the Shuanghu site (XZSH) in Xizang province, located 539 km north of the epicenter, as the reference site.

To mitigate the common-mode errors (Wdowinski et al., 1997; Wang et al., 2007), we implemented an enhanced modified sidereal filtering (Choi et al., 2004) technique combined with a stacking filter approach, utilizing two days of pre-seismic data. This methodology achieved kinematic positioning accuracy of 1.3–2.2 cm horizontally and 3.3–4.9 cm vertically. Given the reduced reliability of vertical components, subsequent analyses prioritize horizontal displacement measurements unless explicitly stated (see Fig. 3).

The temporal evolution of site responses clearly delineates seismic wave propagation kinematics. Sites at comparable epicentral distances manifested contrasting waveform amplitudes across the fault system. For instance, the Zhufeng site (XZZF) in Xizang province, displayed SW motion prior to S-wave arrival, followed by NW deflection, a pattern inversely observed at the eastern Dingjie site (XZDJ) in Xizang province. Maximum co-seismic displacements occurred at sites proximal to the northern rupture propagation path.

Quantitative analysis of horizontal peak ground displacements (PGD) revealed values spanning 35–189 mm, with extrema at XZDX (Dingxi, 417 km NE direction, minimum) and XZSJ (Sajie, 70 km NE direction, maximum). The latter recorded permanent NEE-oriented deformation of ~95 mm attributable to co-seismic effects.

In order to visualize the GNSS site's response to the co-seismic effects of the Dingri M_S 6.8 earthquake more intuitively, we draw a bird's-eye view of the site's motion during the earthquake, which means observing the horizontal motion of the GNSS site during the earthquake from the zenith direction (Fig. 4). The trajectories of XZZF and XZSJ sites demonstrate significant shaking and permanent deformation patterns consistent with normal fault rupture mechanisms. These displacement patterns enable preliminary delineation of the co-seismic impact zone, providing critical constraints for rapid disaster assessment.

5.2. Static deformation characteristics

Static co-seismic displacements were derived from 30 s GNSS data processed using GAMIT/GLOBK, following methodologies in Li et al. (2015, 2021). To ensure reference frame consistency and solution reliability (Wang et al., 2011), we synchronously process ~230 IGS sites around the world, ~40 GNSS sites in Xizang area from 2025-1–4 to 2025-1-7, of which 12 GNSS sites within 400 km of the epicenter only used the time period from UTC 02:00:00 to 24:00:00, 2025-1-7 (the earthquake occurred on 01:05:16 2025-1-7 UTC). Three days data before the earthquake compensated for potential data gaps, while post-seismic analysis limited near-field sites to one-day data to minimize afterslip contamination. The resultant static co-seismic displacement field (Fig. 1, Table 2) exhibits characteristic normal fault extension, correlating with focal mechanism solutions. All sites within 100 km documented pervasive permanent deformation, with XZSJ showing ~95 mm NEE displacement.

Spatial interpolation of horizontal displacements using the slip regression method developed by Shen et al. (1996, 2015) generated continuum strain fields (Fig. 5). Dilatation strain analysis reveals that pronounced tensile deformation west of XDF is consistent with the deformation field induced by InSAR observation (Wang et al., 2025). Asymmetric N-S deformation suggesting predominant northward rupture propagation. The deformation on the south side is not significant after crossing the STDF, suggesting that the southward expansion was limited. It can also be said that the earthquake did not have a significant impact on the area south of the STDF. The maximum shear strain indicates that there was also a slight shear deformation on the west side of the epicenter.

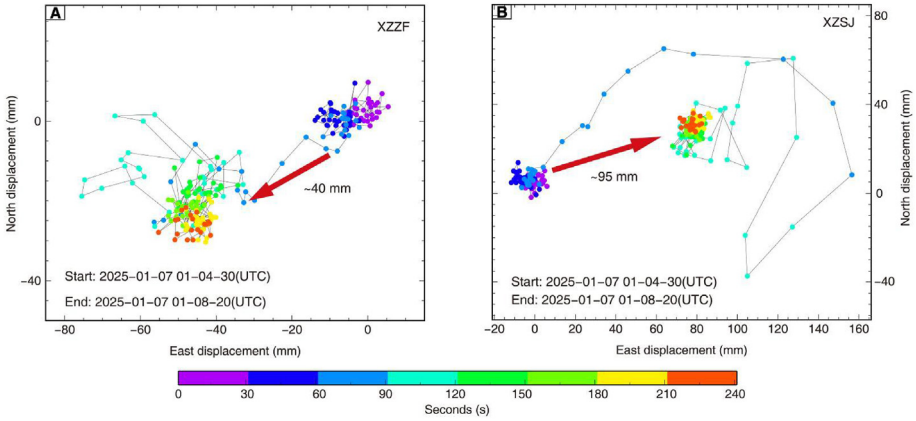

Fig. 4. A bird's-eye view map of GNSS sites during the Dingri earthquake. The x and y-axis denote the displacement of EW and NS components. The color dots represent the horizontal position of the site per second, and the color from blue to red indicates the time. The red arrow in Fig. 4a shows the permanent displacement direction of the XZZF and XZSJ sites due to the Dingri M_S 6.8 earthquake.

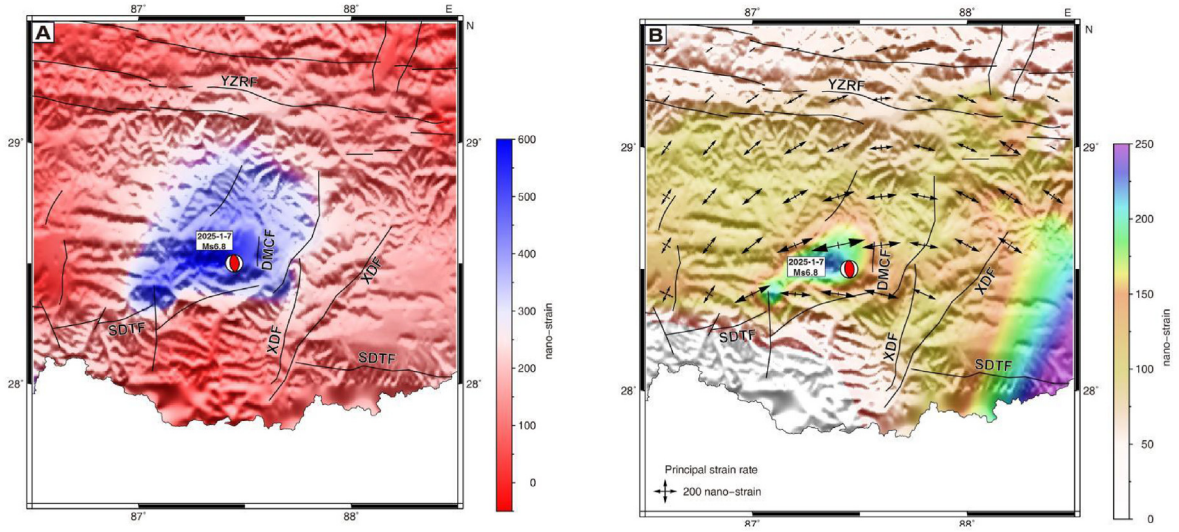

Fig. 5. The co-seismic strain field drived from co-seismic displacement. Fig. 5a and b shows the dilatation, maximum shear strain with the principal strain. Black cross arrow indicates the principal strain drived from co-seismic displacement.

Table 2
Co-seismic displacement of Dingri M_S 6.8 earthquake.

Site	Longitude (°)	Latitude (°)	Epicenter distance (km)	E-W Displacement (mm)	N-S displacement (mm)
LHAS	91.10	29.65	377.66	2.5 ± 1.6	2.6 ± 1.4
XZAR	87.18	29.26	89.27	−8.8 ± 1.5	−0.8 ± 1.3
XZZB	84.15	29.68	345.87	−1.6 ± 1.6	1.7 ± 1.4
XZZF	86.94	28.35	52.24	−41.2 ± 1.8	−14.0 ± 1.6
XZNM	87.23	31.79	367.18	0.1 ± 1.7	1.3 ± 1.5
XZRK	88.86	29.24	160.95	10.4 ± 1.4	5.4 ± 1.2
XZDX	91.09	30.48	417.05	1.6 ± 1.6	2.0 ± 1.4
XZDJ	87.76	28.37	33.72	42.8 ± 4.1	−1.3 ± 3.3
XZJL	85.30	28.86	213.42	−5.8 ± 2.2	2.3 ± 1.9
XZNL	85.97	28.16	149.29	−10.7 ± 3.7	−0.9 ± 2.9
XZSG	85.22	29.32	234.82	−2.7 ± 2.7	2.1 ± 2.3
XZSJ	88.02	28.89	70.69	92.4 ± 3.8	25.7 ± 3.2

6. Discussion and result

In this paper, through the integrated geodetic analysis of the crustal deformation characteristics before and during the Dingri M_S 6.8 earthquake, we found that the distinctive kenematic processes with spatio-temporal heterogeneity in pre-seismic deformation patterns. Moreover, the pre- and co-seismic deformation characteristics are highly consistent with the rupture characteristics of the earthquake source.

(1) GNSS-derived velocity and strain rate fields demonstrate sustained N-S oriented compressive strain accumulation in the epicentral area. In particular, enhanced E-W extensional deformation emerged during the three years pre-seismic period, accompanied by CCW rotation of the principal compressive strain axis. These observations suggest intensified fault activities along the normal faults in this region prior to the mainshock.
(2) Joint analysis of the kinematics and static co-seismic deformation fields reveal significant displacement proximal to the rupture fault. The maximum co-seismic displacement occurs at the XZSJ site, ~70 km northeast of the epicenter, reaching approximately 95 mm. In addition, the seismographic records and co-seismic displacements collectively indicate predominant northeastward rupture propagation, with deformation patterns exhibiting a clear normal faulting mechanism consistent with the rupture characteristics of the hypocenter.
(3) The co-seismic strain distribution analysis shows localized strain release concentrated west of the XDF and north of STDF structures. While the immediate strain release area appears limited, the potential triggering effects on adjacent N-S trending normal fault systems require systematic evaluation through continued monitoring.

CRediT authorship contribution statement

Yu Li: Writing – review & editing, Writing – original draft, Software, Project administration, Methodology, Funding acquisition, Data curation. **Yuebing Wang:** Resources, Methodology, Data curation, Conceptualization. **Yinxing Shao:** Software, Data curation. **Hongbo Shi:** Validation, Funding acquisition. **Tan Wang:** Resources, Data curation.

Declaration of competing interest

The authors declare that they have no known competing financial interests or personal relationships that could have appeared to influence the work reported in this paper.

Author agreement and acknowledgment

All authors agree for this publication. I am grateful to all the contributors to GAMIT/GLOBK software. GAMIT/GLOBK provides free download of authorization (http://geoweb.mit.edu/). The figures were drawn by GMT (Wessel et al., 2013). Many thanks to the reviewers and editor-in-chief for their valuable feedbacks. This work was supported by grants from the National Natural Science Foundation of China (42374010, 42004010).

References

Altamimi, Z., Metivier, L., Rebischung, P., Collilieux, X., Chanard, K., Barnéoud, J., 2023a. ITRF2020 plate motion model. Geophys. Res. Lett. 50 (24), e2023GL106373.
Altamimi, Z., Rebischung, P., Collilieux, X., Métivier, L., Chanard, K., 2023b. ITRF2020: an augmented reference frame refining the modeling of nonlinear site motions. J. Geod. 97 (5), 47.
Bock, Y., Melgar, D., 2016. Physical applications of GPS geodesy: a review. Rep. Prog. Phys. 79 (10), 106801.
Choi, K., Bilich, A., Larson, K.M., Axelrad, P., 2004. Modified sidereal filtering: implications for high-rate GPS positioning. Geophys. Res. Lett. 31 (22).
Crotwell, H.P., Owens, T.J., Ritsema, J., 1999. The TauP Toolkit: Flexible seismic travel-time and ray-path utilities. Seismol Res. Lett. 70, 154–160.

Herring, T.A., King, R.W., Floyd, M.A., McClusky, S.C., 2018. GAMIT Reference Manual: GPS Analysis at MIT. Release 10.70. Department of Earth, Atmospheric, and Planetary Sciences. Massachusetts Institute of Technology.

Jackson, D.D., Shen, Z.K., Potter, D., Ge, X.B., Sung, L.Y., 1997. Southern California deformation. Science 277 (5332), 1621–1622.

Li, Y., 2021. Analysis of GAMIT/GLOBK in high-precision GNSS data processing for crustal deformation. Earthquake Research Advances 1 (3), 100028.

Li, Y., Liu, J., Liang, H., Zhang, R., Shi, H.B., Wang, P., et al., 2015. Co-seismic displacement field associated with the 25 April, 2015 M W 7.8 Nepal earthquake recorded by Global Positioning System. Chin. Sci. Bull. 60, 3606–3616.

Li, Y., Wang, Y., Zhao, L., Shi, H., Wang, P., 2024. Kinematic deformation and intensity assessment of the 2021 Maduo M_S 7.4 earthquake in Qinghai revealed by high-frequency GNSS. Geodesy and Geodynamics 15 (3), 230–240.

Liu, J., Ji, C., Zhang, J., Zhang, P., Zeng, L., Li, Z., Wang, W., 2015. Tectonic setting and general features of co-seismic rupture of the 25 April, 2015 Mw 7.8 Gorkha, Nepal earthquake. Chin. Sci. Bull. 60, 2640–2655.

Nikolaidis, R., 2002. Observation of Geodetic and Seismic Deformation with the Global Positioning System. University of California, San Diego.

Shen, Z.K., Jackson, D.D., Ge, B.X., 1996. Crustal deformation across and beyond the Los Angeles basin from geodetic measurements. J. Geophys. Res. Solid Earth 101 (B12), 27957–27980.

Shen, Z.K., Wang, M., Zeng, Y., Wang, F., 2015. Optimal interpolation of spatially discretized geodetic data. Bull. Seismol. Soc. Am. 105 (4), 2117–2127.

Shen, Z.K., Zhao, C., Yin, A., Li, Y., Jackson, D.D., Fang, P., Dong, D., 2000. Contemporary crustal deformation in east Asia constrained by Global Positioning System measurements. J. Geophys. Res. Solid Earth 105 (B3), 5721–5734.

Sheng, S.Z., Wan, Y.G., Jiang, C.S., Bu, Y.F., 2015. Preliminary study on the static stress triggering effects on China mainland with the 2015 Nepal M_S 8.1 earthquake. Chin. J. Geophys. 58 (5), 1834–1842.

Shi, F., Liang, M.J., Luo, Q.X., Qiao, J.X., Zhang, D., Wang, X., Yi, W.X., Zhang, J.W., Zhang, Y.F., Zhang, H.P., Li, T., Li, A., 2025. Seismogenic fault and co-seismic surface deformation of the Dingri Ms 6.8 earthquake in Tibet, China. Seismol. Geol. 47 (1), 1–15.

Tapponnier, P., Peltzer, G.L.D.A.Y., Le Dain, A.Y., Armijo, R., Cobbold, P., 1982. Propagating extrusion tectonics in Asia: new insights from simple experiments with plasticine. Geology 10 (12), 611–616.

Wang, G.Q., Boore, D.M., Tang, G., Zhou, X., 2007. Comparisons of ground motions from colocated and closely spaced one-sample-per-second global positioning system and accelerograph recordings of the 2003 M 6.5 San Simeon, California, earthquake in the Parkfield region. Bull. Seismol. Soc. Am. 97 (1B), 76–90.

Wang, M., Shen, Z.K., 2020. Present-day crustal deformation of continental China derived from GPS and its tectonic implications. J. Geophys. Res. Solid Earth 125 (2), e2019JB018774.

Wang, M., Li, Q., Wang, F., Zhang, R., Wang, Y., Shi, H., et al., 2011. Far-field co-seismic displacements associated with the 2011 Tohoku-oki earthquake in Japan observed by Global Positioning System. Chin. Sci. Bull. 56, 2419–2424.

Wang, N., Li, Y.S., Shen, W.H., Jiang, W.L., Li, Q., Jiao, Q.S., 2025. Source parameters and rapid simulation of strong ground motion of the M_S 6.8 earthquake on January 7, 2025 in Dingri (Xizang, China) derived from InSAR observatioin. Geomatics Inf. Sci. Wuhan Univ. https://doi.org/10.13203/J.whugis20250022.

Wdowinski, S., Bock, Y., Zhang, J., Fang, P., Genrich, J., 1997. Southern California permanent GPS geodetic array: spatial filtering of daily positions for estimating co-seismic and postseismic displacements induced by the 1992 Landers earthquake. J. Geophys. Res. Solid Earth 102 (B8), 18057–18070.

Wessel, P., Smith, W.H., Scharroo, R., Luis, J., Wobbe, F., 2013. Generic mapping tools: improved version released. Eos, Transactions American Geophysical Union 94 (45), 409–410.

Whaley, I.I.I.D.L., 2005. The Interquartile Range: Theory and Estimation (Master's Thesis. East Tennessee State University.